Materials Science & Engineering A 832 (2022) 142367

Contents lists available at ScienceDirect

Materials Science & Engineering A

journal homepage: www.elsevier.com/locate/msea

A framework for predicting the local stress-strain behaviors of additively manufactured multiphase alloys in the sequential layers

Siqi Liu [a], Meichao Lin [a], Xu Wang [a,b], Yuequn Fu [a], Xiaobo Ren [c], Zhiliang Zhang [a], Jianying He [a,*]

[a] NTNU Nanomechanical Lab, Department of Structural Engineering, Norwegian University of Science and Technology (NTNU), Trondheim, 7491, Norway
[b] College of Safety and Ocean Engineering, China University of Petroleum, Beijing, 102249, China
[c] Materials and Nanotechnology, SINTEF Industry, NO-7465, Trondheim, Norway

ARTICLE INFO

Keywords:
Wire-arc additive manufacturing
Superduplex stainless steel
Stress-strain relationship
Nanoindentation
Microstructure-based FEM

ABSTRACT

The additive manufacturing (AM) process often results in non-uniform microstructure and different mechanical properties in sequential layers, impacting the overall performance of the AM-ed component. However, it is extremely challenging to evaluate the local stress-strain behavior of each individual layer, owing to the limited size of the AM-ed layered structure. To this end, a framework for characterizing and predicting the mechanical evolution of AM-ed multiphase alloys by combing nanoindentation and microstructure-based finite element method (FEM) was proposed. The sample used in this study was superduplex stainless steel (SDSS) manufactured by wire arc additive manufacturing (WAAM), and the microstructure varied from layer to layer. Firstly, the mechanical properties of the two constituent phases in each layer, including elastic modulus and hardness, were obtained by nanoindentation, and the indentation size effect (ISE) was also evaluated. The yield strength and hardening exponent of each phase were subsequently estimated by reverse analysis method, and therefore the constitutive behaviors of the individual phase, which served as input parameters for FEM, were acquired. By aid of real microstructure-based FEM under uniaxial tension, the overall stress-strain behaviors of each layer and the distributions of the stress and strain during the deformation process were investigated. This work provides a new avenue for the characterization of the multiphase alloys in AM industry, beneficial to the understanding of the mechanical evolution in AM-ed materials.

1. Introduction

In recent years, metal additive manufacturing technology has gathered numerous scientific and technological interests for the new revolution of the manufacturing field. Additive manufacturing (AM), also known as the 3D printing technique, is a process based on layer-upon-layer manufacturing [1–3]. The application of AM in the manufacturing field is promising owing to its distinctive superiorities, including the flexibility of shape design, the rapidity of fabrication, and the tunability of material properties [4–6]. Wire and arc additive manufacturing (WAAM), as one kind of the directed energy deposition (DED) processes, is an AM method to build components by utilizing a welding wire as feedstock and using arc to provide heat source [7–9]. On account of the complex thermal history during the WAAM process, the metallic materials experience varying thermal cycles, which results in the non-equilibrium microstructures and therefore the inhomogeneous mechanical properties [10].

Having great insight into the evolution of mechanical properties in sequential layers during AM process is significant for optimizing the mechanical properties of AM-ed materials and further industrial applications. However, there are few studies devoted to this topic for the time being. In the majority of the previous research, conventional testing methods, such as tensile and compression, have been widely used for measuring the macroscale mechanical properties of AM-ed materials [11–16]. Nevertheless, the highly inhomogeneous microstructures and the complexity of the shape in some AM components that lead the conventional methods to be inapplicable for the exploration of the mechanical properties in a constrained size. Nanoindentation, a method that operates in the nano or sub-micron depth with nanoscale resolution, makes it possible to investigate the local mechanical properties of sequential layers in an AM-ed material. What's more, a large number of research efforts have been made in the development of

* Corresponding author.
E-mail address: jianying.he@ntnu.no (J. He).

https://doi.org/10.1016/j.msea.2021.142367
Received 23 July 2021; Received in revised form 18 November 2021; Accepted 19 November 2021
Available online 24 November 2021

nanoindentation-based methods to extract the stress-strain relationship and the plastic properties including the yield strength and the strain-hardening exponent. There are mainly two approaches for the stress-strain behavior by nanoindentation. The first approach is to determine the stress-strain curve directly from the load-displacement curve by spherical nanoindentation testing [17–19]. The other one is the reverse analysis method based on dimensionless functions, where the elastoplastic parameters of the material's constitutive behavior are inversely deduced from the load-displacement curve [20–24]. Consequently, the local constitutive behaviors of specific locations in the AM deposition wall can be achieved.

It is well accepted that the mechanical properties of the multiphase metallic materials are affected by not only the properties of the individual constituent phase but also the morphology and volume fraction of the constituent phases in the microstructure [25]. Most of the published reports put forward the approach for investigating the impact of individual phases on the macroscopic mechanical properties, by utilizing the nanoindentation method to quantify the mechanical properties of the constituent phases and subsequently performing tensile tests to acquire the overall mechanical properties [26–28]. This approach is appropriate for some multiphase materials, where the tension specimen can be representative of the overall sample. Nevertheless, it is inapplicable for AM-ed materials because the microstructure show heterogeneity in sequential layers and it is challengeable for conventional tensile tests to be performed in a limited size (such as in individual layer). Instead of tensile tests, the finite element method (FEM) on the basis of the real microstructure can be an appropriate option to explore the constitutive behaviors in a constrained location of AM-ed multiphase materials. In addition, this approach can obtain not only the stress-strain behavior but also the stress-strain distributions and failure initiation during the deformation process [29].

Superduplex stainless steel (SDSS) is a kind of steel that has a nearly equal percentage of ferritic-austenitic microstructure, where the ferrite is a body-centered cubic (bcc) structure and austenite is a face-centered cubic (fcc) structure [30]. SDSS is widely applied in the petroleum and gas industry due to its high strength and excellent corrosion resistance. The application of AM in manufacturing SDSS has gained great attention in recent years [30–32]. Therefore, SDSS is used as the representative multiphase material for studying the proposed framework in the current work.

In an effort to investigate the local stress-strain behavior of the layered structure in AM-ed alloys and establish the correlation between constituent phases and macroscale mechanical properties, we propose a framework combining nanoindentation and finite element method in the current study. SDSS manufactured by WAAM was utilized in this work. The mechanical properties of the austenite and ferrite phases in different layers of this material were characterized by nanoindentation, and the constitutive behaviors of the individual phase are extracted and used as the input parameters for FEM. The actual microstructures of SDSS were then observed by optical microscopy, and then used to build the corresponding FEM models. The overall constitutive behaviors of each layer were subsequently investigated by FEM under uniaxial tension. It is hoped that this work will lead to new insights into the characterization of the multiphase alloys in AM industry and the optimization of the mechanical properties of AM-ed materials.

2. Experimental methods and FEM model

2.1. Sample preparation

The sample studied in the current work came from one piece of wire-arc additive manufactured 2507 superduplex stainless steel, with the elemental composition shown in Table S1 and the deposition parameters shown in Table S2. The current wall depositions constituted 17 layers, and the average layer height was about 2.0–2.6 mm. The sample was cut from the top with the size of 1cm × 1cm × 0.5 cm, as illustrated in Fig. 1,

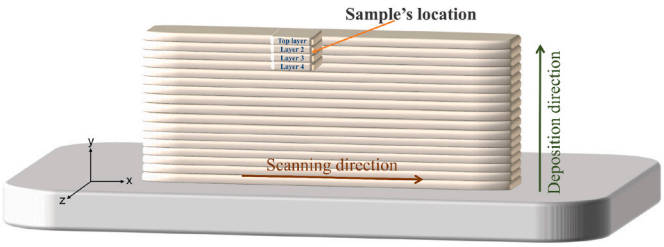

Fig. 1. Sketch map of the wall of the weld.

including totally four layers. The examined surface of the sample (x-y plane) was ground and mechanical polished, and then electrolytically etched in a mixed solution of HNO_3:H_2O = 1:1 to remove the surface strain caused by mechanical polishing and obtain good contrast between austenite (γ) and ferrite (α) [33].

2.2. Material assessment methods

The microstructures were observed by Olympus BX51 Polarized Light Microscope, and the austenite and ferrite phase fractions were evaluated by the image analysis using ImageJ software. The volume fractions were determined by using five optical micrographs in each layer to get the average values. The nanomechanical characterization of the specimen was conducted by using the nanoindentation method with Hysitron Tribo-indenter TI 950 equipped with a Berkovich indenter tip. The mode used for the investigation of hardness and elastic modulus was a load-controlled mode with a maximum load of 6 mN and a constant loading rate of 0.5 mN/s. At least 10 indents were performed on each phase in different layers to obtain the average value, and all the indents fell into the interior of each phase in order to avoid the influence of phase boundary. The load function used for exploring the indentation size effect (ISE) was the partial unloading function that contains 20 cycles with a maximum load of 10 mN, as illustrated in Fig. S1.

2.3. Creating the FEM models

The FEM models were based on the representative areas (70 μm × 70 μm) optically observed from the four layers. The volume fractions of ferrite in the representative areas were consistent with the experimental results shown in the following section. The models were built strictly following the microstructure features displayed in Fig. 2(a). It was achieved by extracting the path of phase boundaries from the optical microscopy images and then importing the path into ABAQUS. The plane stress quadrilateral elements were utilized in all FEM analyses. The developed meshing strategy was well applied in the microstructure-based FEM models and comparable with the reported pixel-based meshing strategy for segmented structures [34,35]. All the models were meshed with about 100000 elements of the type CPS4, and the representative zoom-in view of selected finite element mesh was presented in Fig. 2(c). The load was applied to the top side and bottom side in the y-direction, as shown in Fig. 2(b). Uniaxial tension simulation was performed on each layer until failure. Representative stress-strain curves obtained from the nanoindentation test and reverse analysis method, seen in Fig. 6, were served as inputs for calculation.

3. Results and discussion

3.1. Microstructure evolution

The multilayer structure of AM-ed materials is likely to be heterogeneous due to the features of AM method, which is expected to influence the mechanical property of the material. Fig. 3 displays the representative optical metallography of the four layers of the sample: (a_1) and (a_2) show the microstructure of the Top layer at different

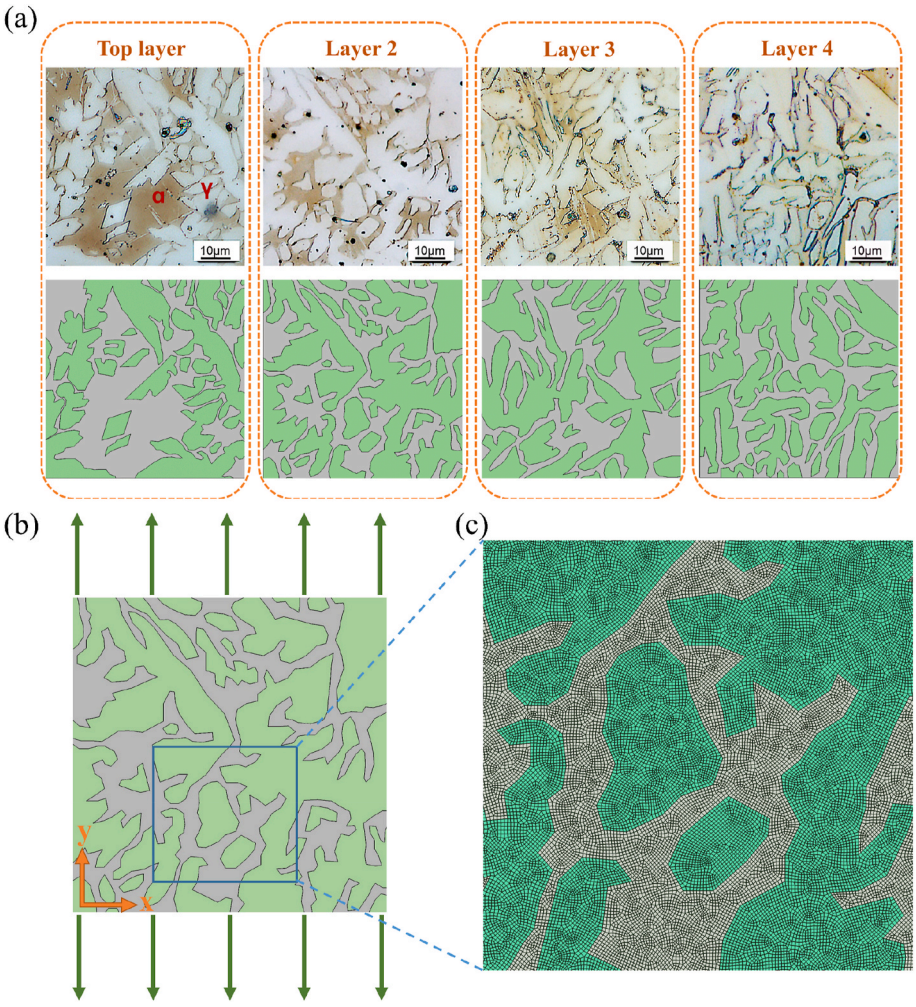

Fig. 2. (a) The actual microstructures in the four layers and the corresponding sketches of the FEM models; (b) the sketch map of the load direction of uniaxial tension; (c) the representative finite element mesh of the selected partial area from the blue rectangle in (b). (For interpretation of the references to colour in this figure legend, the reader is referred to the Web version of this article.)

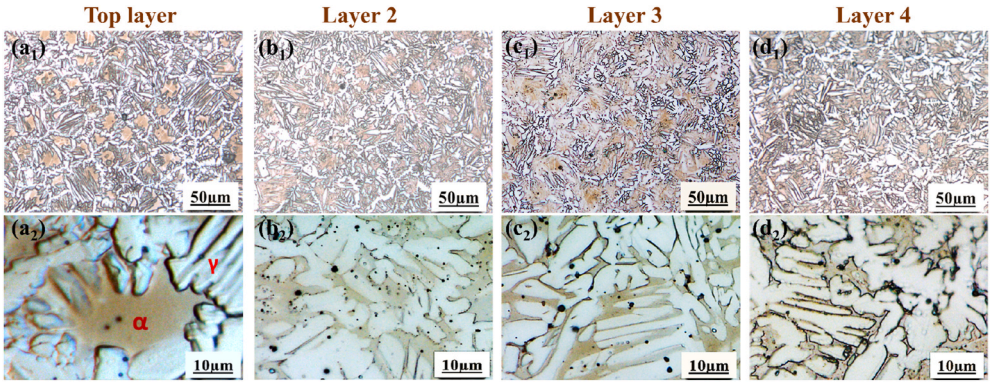

Fig. 3. Representative microstructures of different layers in the sample by means of optical metallography: (a_1) (b_1) (c_1) (d_1) show the microstructure of the four layers; (a_2) (b_2) (c_2) (d_2) exhibit a higher magnification image of the microstructures of the four layers. The bright and white phase is austenite (γ), and the yellow phase is ferrite (α). (For interpretation of the references to colour in this figure legend, the reader is referred to the Web version of this article.)

magnification separately; (b_1) and (b_2) illustrate the microstructure of the second layer (Layer 2); the third (Layer 3) and fourth layer's (Layer 4) are shown in (c_1) (c_2) and (d_1) (d_2) respectively. Austenite (γ) appears bright, while ferrite (α) is relatively dark, as addressed by a magnetic force microscope in the previous work [36,37]. Furthermore, the microstructure evolution on each layer can be observed in Fig. 3. What's more, the ratio of the two phases varies somewhat in the four layers. The percentage of austenite and ferrite are listed in Table 1, indicating that the ratio of austenite in Top layer is much lower than that of the others and there is a slight increase from Layer 2 to Layer 4. This observation agrees with several reported studies [7,10,38], and it suggests that the evolution of the austenite volume fraction is relevant to the repeated

Table 1
The percentage of austenite and ferrite in the four layers.

	Top layer	Layer 2	Layer 3	Layer 4
Austenite	47 ± 3%	61 ± 1%	62 ± 2%	63 ± 1%
Ferrite	53 ± 2%	39 ± 1%	38 ± 2%	37 ± 2%

reheating during the layer-upon-layer deposition process. The reheating process can result in an increased cooling time and the repeated dwell time within the range of 800–1200 °C where the ferrite may transform to austenite [31]. Since there is a reheating effect on the layers except for Top layer, the microstructure evolution in this sample is largely attributed to the effect of the complex thermal cycles and cooling rate during the WAAM process.

3.2. Mechanical properties of individual phase characterized by nanoindentation

3.2.1. Hardness and elastic modulus

The local nanomechanical properties of austenite and ferrite phases in different deposition layers were characterized by using the nanoindentation technique. The hardness and elastic modulus are the two fundamental mechanical properties characterized by nanoindentation, and they can be calculated by the widely-accepted Oliver and Pharr (O–P) methods [39,40].

Fig. 4 (a) and (b) show the average values of hardness and elastic modulus in each layer of the sample. Firstly, by comparing the results between ferrite and austenite, both the elastic modulus and hardness of austenite are larger than those of ferrite. These findings are in contrast with the previous studies where the ferrite was found to have higher nano-hardness and elastic modulus [29,41,42], and this is most likely attributable to the indentation size effect which will be discussed below. Furthermore, it can be found that there exist variations in the hardness and elastic modulus of the four layers, indicating that the complex WAAM process has obvious influences on the mechanical properties of each phase. The variation of the hardness is not very significant, and the averaged hardness values of both phases in Layer 2 are the largest, followed by Layer 3 and then Top layer, Layer 4. There are great differences in the elastic modulus in different layers, where the mean value of elastic modulus in Top layer is the largest, then followed by Layer 2, Layer 3, Layer 4, and the difference between the two extremes is more than 50 GPa. Therefore, the AM process has a greater impact on the elastic modulus of SDSS than hardness. It should be pointed out that the tendencies of hardness and elastic modulus in Layer 2, Layer 3, and Layer 4 are similar, that is, all of the values decrease from Layer 2 to Layer 4. This may be attributed to the thermal history that can influence the heat dissipation and cooling rate, and Layer 4 experiences the maximum number of thermal cycles. The varying cooling rate has an impact on the microstructure including the dislocation density, grain size, and precipitation distribution, etc., and further affects the mechanical properties [10,12,43]. However, Top layer is the special case that this layer does not experience the effects of reheating, and it has a higher cooling rate than other layers since it is in direct contact with the air after deposition. It may be difficult to reach any conclusion with regard to the exact reasons for this trend, and there are insufficient microstructure analyses (void, precipitate, dislocation density, etc) to determine this aspect. The underlying mechanism of this result merits a detailed study in the next work. The current manuscript is focusing on only four layers, and the main objective of this study is to provide a new framework for the characterization of the non-uniform AM-ed materials. Future studies on other representative locations of the deposition wall will be pursued to figure out the effects of AM process and induced microstructure.

3.2.2. Indentation size effect (ISE)

It is generally accepted that the hardness measured at the nanoscale is dependent on indentation depth, namely the indentation size effect (ISE) [44]. The most widely used model to quantify and analyze the ISE in crystalline materials is the Nix-Gao model which is based on the strain gradient theory [44,45]. Smaller indents have higher strain gradients relative to the size of the plastic zone. According to the strain gradient theory, the density of geometrically necessary dislocations (GNDs) is higher under smaller indentation depth, and then the additional GNDs further increase the flow stress and therefore the hardness. The Nix-Gao model proposed the relation indicating the variation of hardness (H) versus the indentation depth (h), expressed as follows:

$$\frac{H}{H_0} = \sqrt{1 + \frac{h^*}{h}} \tag{1}$$

where H_0 is the hardness in the infinite depth and it represents the macroscopic hardness due to the statistically stored dislocations (SSDs), h^* is a characteristic depth parameter that depends on the material parameters and geometric parameters of the indenter. This equation can be rewritten as:

$$H^2 = H_0^2\left(1 + \frac{h^*}{h}\right) \tag{2}$$

Therefore, H_0 and h^* can be obtained by using this equation to fit the experimental data.

The representative curves showing hardness as a function of the displacement in the four layers are presented in Fig. 5(a)(b)(c)(d), where the values of hardness exhibit the obvious size effect. According to Eq. (2), the plots of H^2 versus $1/h$ in the four layers are shown in Fig. 5(e)(f)(g)(h), and they exhibit linearity which means the indentation size effect is active for this material. However, H^2 data show a little bit of scattering when the displacement is smaller than 100 nm, and the reason is likely to be the surface effect and imperfect indenter geometry [46]. From the

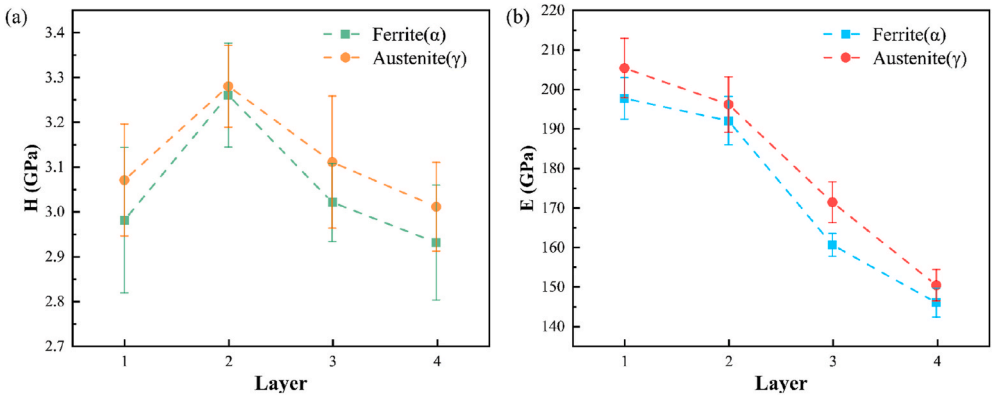

Fig. 4. Hardness and modulus in different layers of the sample. (a) The hardness of the four layers, (b) Elastic modulus of the four layers of the sample.

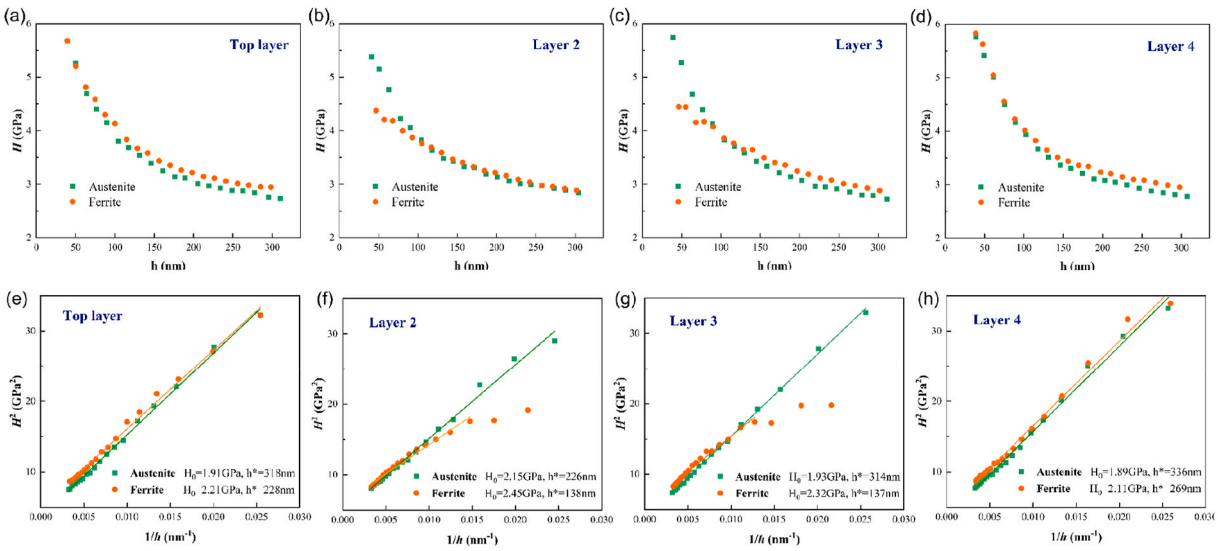

Fig. 5. Indentation displacement dependence of hardness in (a) Top Layer, (b) Layer 2, (c) Layer 3, (d) Layer 4. The fitting curve by using Nix-Gao model in (e) Top Layer, (f) Layer 2, (g) Layer 3, (h) Layer 4.

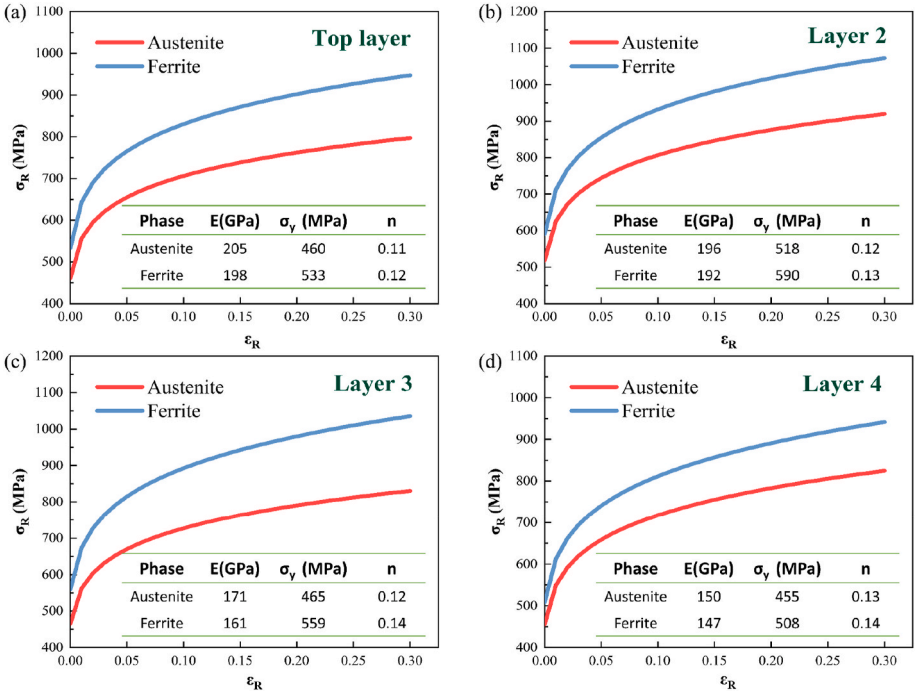

Fig. 6. Representative stress-strain (ε_R $-\sigma_R$) curves of ferrite and austenite in (a) Top layer, (b) Layer 2, (c) Layer 3, (d) Layer 4.

fitted curve, the values of H_0 and h^* are calculated as shown in Fig. 5 and Table 2. All of the results indicate that the ferrite has relatively higher H_0 and h^* than austenite, and the results suggest that the hardness arisen from the SSDs is higher for the ferrite. Furthermore, the higher values of h^* in austenite verify that the hardness of austenite is much more dependent on the indentation depth than that of ferrite, which is the reason why the difference between the two phases varies with the indentation depth. On the other side, by comparing the results of the four layers, the value of H_0 in Layer 2 is the largest, and then is Layer 3, followed by Top layer, Layer 4, which is consistent with the trend of results in Fig. 4(a). This result further confirms the location dependence of hardness in the WAAM process.

Table 2
Summary of the values of H_0 and h^* calculated by Nix-Gao model in the four layers.

	Top layer		Layer 2		Layer 3		Layer 4	
	Austenite	Ferrite	Austenite	Ferrite	Austenite	Ferrite	Austenite	Ferrite
H_0 (GPa)	1.91	2.21	2.15	2.45	1.93	2.32	1.89	2.11
h^* (nm)	318	228	236	138	314	137	336	269

3.2.3. Yield strength and hardening exponent

Besides elastic modulus, the yield strength and strain-hardening exponent are the other two critical parameters for determining the constitutive behavior of metallic materials. For the non-homogeneous or multi-phase material, the conventional tensile method for extracting local yield strength and strain hardening exponent of individual phase is not applicable anymore. Several research efforts have been devoted to investigating the local stress-strain behavior of individual phases through nanoindentation [26,47,48]. Even though Tabor's empirical law has provided the expression correlated the hardness and yield properties ($H = c\sigma$), the relationship is not appropriate in low indentation depth at nanoscale owing to the ISE [49]. One previous work by Rodríguez and Gutierrez [50] took the ISE into account and investigated the relationship between the nanoindentation results and yield strength of the tensile tests. Furthermore, an inverse analysis approach proposed by Ma et al. [51] for the Berkovich tip is widely accepted. Herein, we adopt the empirical relations proposed by Rodríguez and Gutierrez [50] for estimating the yield strength (σ_y) and an inverse analysis model developed by Ma et al. [51] for extracting the values of the hardening exponent (n), described as bellows:

$$H_0 = 4.15\sigma_y \tag{3}$$

$$\frac{H_0}{\sigma_y} = f\left(n, \frac{\sigma_y}{E}\right) = \left(1.76 - 3.70n + 2.52n^2\right)\cdot\left(\frac{\sigma_y}{E}\right)^{(-0.073-0.96n)} \tag{4}$$

Here, the estimated values of σ_y and n of each phase in the four layers are displayed in Table 3.

In order to obtain the power-law stress-strain curve from nanoindentation, the representative strain and representative stress that defined by Dao et al. [52] are expressed as follows:

$$\varepsilon_R = \varepsilon - \sigma_y/E \tag{5}$$

$$\sigma_R = \sigma_y\left(1 + \frac{E}{\sigma_y}\varepsilon_R\right)^n \tag{6}$$

where ε_R is the representative strain, ε is the uniaxial strain, and σ_R is the representative stress. According to the suggested procedure above with the determined parameters, the representative stress-strain curves of each phase in the four layers are obtained, as presented in Fig. 6. These properties of the individual constituent phase serve as the input parameters for the following FEM simulations.

3.3. Stress-strain behaviors by FEM

The prediction of the overall stress-strain behavior of each layer is investigated by the FEM with the plane stress elements under uniaxial tension.

The exploration of the distributions of the stress and strain of the SDSS are exhibited in Fig. 7 and Fig. 8, and thus the contributions of each constitute phase to the overall behavior can be figured out. Fig. 7 presents the contours of von Mises stress and equivalent plastic strain at the applied nominal strain of 7.68% in the four layers, and the black contour lines inside the figures are used to better distinguish the distributions of ferrite and austenite. As shown in Fig. 7(a)(b)(c)(d), the distributions of von Mises stress indicate that the ferrite has higher stress than the austenite in each layer, and the higher stresses appear in the small localized region of the ferrite phases. Furthermore, the distribution of von Mises stress in Layer 2 shows the highest value among the four layers, and the maximum stress with 7.68% applied strain in Layer 2 is 985 MPa. Besides, the von Mises stress of Layer 3 is the second-highest, followed by Top layer and Layer 4. On the other side, as can be seen from Fig. 7 (e)(f)(g)(h), the higher equivalent plastic strain occurs in the austenite of each layer, owing to its lower yield strength [53,54]. Furthermore, the maximum equivalent plastic strain in each layer is much higher than the applied strain, owing to the effect of phase morphology and localized plasticity, and the maximum equivalent plastic strain in the Top layer is the largest. To compare the stress and strain response of the two phases quantitatively, the mean values of stress and strain are calculated and the ratios in the form of $\sigma_\gamma/\sigma_\alpha$ and $\varepsilon_\gamma/\varepsilon_\alpha$ are determined, as shown in Table 4. The distributions of the stress and strain show great heterogeneity, which can be attributed to the distinction of the plastic properties in the two phases. The ferrite sustains more stress because the ferrite has higher yield strength and can resist plastic deformation more than the austenite.

In order to examine the evolution of the stress and strain distributions during the deformation process, the FEM results in Layer 4, including the obtained engineering stress-strain curve and the distributions of von Mises stress and equivalent plastic strain at three representative applied engineering strain levels, are shown in Fig. 8. Point *a*, at the applied strain of 0.38%, represents the state before yielding, and this state is under the elastic deformation stage and both phases deform elastically [53]. Point *b*, at a strain level of 7.68%, belongs to the plastic deformation stage, and it is located after the yielding and before the failure occurs. At this stage, the plastic deformation has spread, and the strain-localized area looks more extensive than that of the elastic stage. Point *c* indicates the state that the material begins to fail, strain localized area decreases but the average strain in this area increases. Obviously, the strain localization band, which is considered to be the early stage of failure/fracture zone [55], becomes more visible with the increasing applied strain levels.

Strain localization factor (SLF), which is a factor to reveal the level of strain localization quantitively, is described as [54]:

$$\mathrm{SLF} = \sum_{i=1}^{n}\left(\varepsilon_{i,A}F_{i,A} - \varepsilon_{i,F}F_{i,F}\right) \tag{7}$$

where $F_{i,A}$ and $F_{i,F}$ are the area frequency of $\varepsilon_{i,A}$ and $\varepsilon_{i,F}$; $\varepsilon_{i,A}F_{i,A}$ and $\varepsilon_{i,F}F_{i,F}$ are the equivalent plastic strain of i-th bin for austenite and ferrite, respectively.

The curves of probability distribution function (PDF) of equivalent plastic strain in Layer 4, as shown in Fig. 9, provide quantitative information of the strain distributions. The curves verify that the plastic strain of austenite is larger than that of ferrite and the plastic strain increases with the applied strain. Furthermore, the corresponding SLF under three representative applied strain levels are calculated. The tendency of the results of SLF demonstrates that the degree of strain localization increases with the applied strain levels.

The overall engineering stress-strain curves of the four layers obtained by FEM simulation are shown in Fig. 10. The overall mechanical property, the bulk elastic moduli and yield strength of each layer, are exacted from these engineering stress-strain curves shown in Table 5. It shows that Top layer has the highest elastic modulus and the yield strength of Layer 2 is the largest. All of the simulated overall values of elastic moduli and yield strength in FEM are between the values of ferrite and austenite in each layer as shown in Table 3. The trends of the

Table 3
The estimated values of yield strength (σ_y) and strain hardening exponent (n) of each phase in the four layers.

	Top layer		Layer 2		Layer 3		Layer 4	
	Austenite	Ferrite	Austenite	Ferrite	Austenite	Ferrite	Austenite	Ferrite
σ_y (MPa)	460	533	518	590	465	559	455	508
n	0.11	0.12	0.12	0.13	0.12	0.14	0.13	0.14

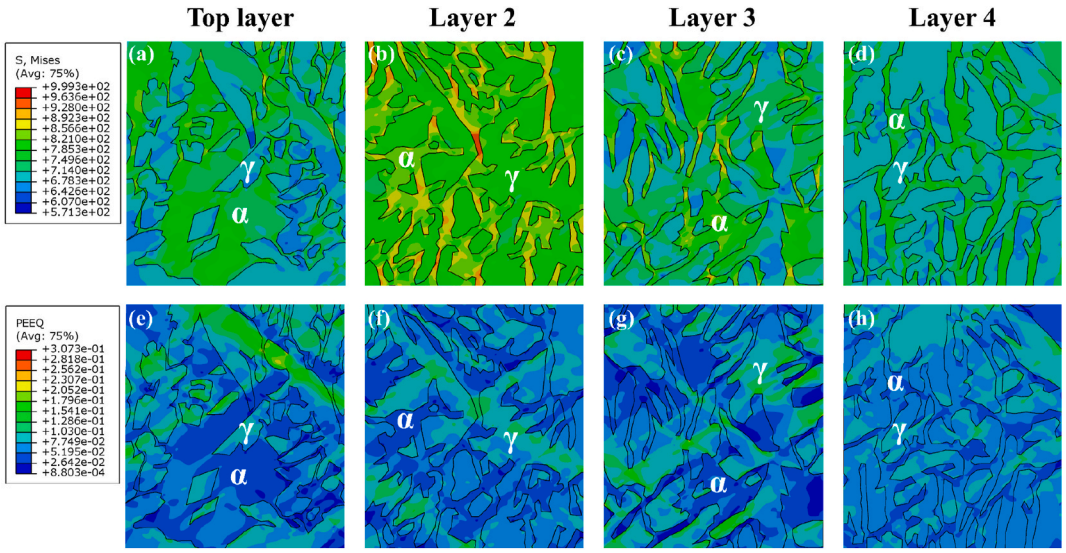

Fig. 7. Contour plots of von Mises stress and equivalent plastic strain under uniaxial tensile with 7.68% applied strain in (a)(e) Top layer, (b)(f) Layer 2, (e)(g) Layer 3, (d)(h) Layer 4.

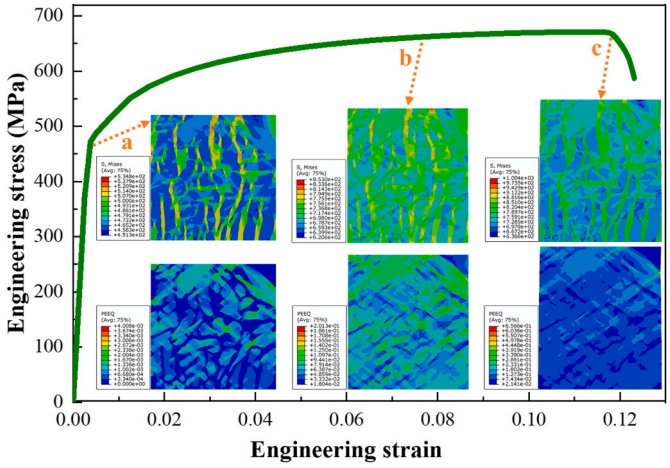

Fig. 8. Engineering stress-strain curve of Layer 4, as well as the distributions of von Mises stress and Equivalent plastic strain under three representative engineering strain levels of (a) 0.38%, (b) 7.68%, (c) 11.43%.

results in FEM show a good agreement with the results of nanoindentation tests for individual phases. This arises from the fact that the difference between the four layers is much greater than the difference between ferrite and austenite in each layer. In other words, the differences in the mechanical properties between the four layers play a dominant role in the FEM results. Moreover, the failure of Top layer first appears, then Layer 3, Layer 2 begin to fail, and the last one is Layer 4, as the failure strain values are shown in Table 5. The strain localization can be regarded as the early stage of the failure process, therefore, the values of SLF at the failure point are calculated for the reflection of strain localization. It is noteworthy that the trend of failure follows the opposite trend of yield strength except Layer 4. Although Layer 4 has the smallest yield strength, the SLF of Layer 4 is much smaller than that of other layers, which means it is less likely to fail. As a consequence, the failure mechanism is not only influenced by plastic deformation including the yield strength and hardening exponent, but also the other causes such as phase morphology and strain localization.

In order to compare the tensile results from the experiment and simulation, actual tensile tests are needed. Due to the experimental limitation of the actual tensile tests on the single layer, the actual tensile test on the specimen constituted all 17 layers was performed to obtain the macroscopic tensile property of the AM-ed material. In addition, a new FEM model that contained the four layers was set up to obtain the overall stress-strain response of the top four layers. The comparison results are presented in Fig. S2 of the supplementary material, implying the methodology we established in this work can be considered credible, and the framework proposed in the current work can be regarded as an easy and reliable method for predicting the local stress-strain behaviors.

4. Conclusion

In this study, nanoindentation tests and microstructure-based finite element modeling (FEM) are combined to extract the nanomechanical properties and predict the stress-strain behavior in each layer of the additively manufactured (AM-ed) superduplex stainless steel (SDSS). We use the nanoindentation test to obtain the local mechanical properties of the individual phase in each layer, then FEM was used to investigate the overall mechanical behavior of each layer. The results can be summed up as follows:

(1) The microstructures of the AM-ed sample indicate that the morphology and volume fractions of the constituent phases are

Table 4
The mean values of von Mises stress and equivalent plastic strain under the uniaxial tensile with 7.68% applied strain, and ratios of the form $\sigma_\gamma/\sigma_\alpha$ and $\varepsilon_\gamma/\varepsilon_\alpha$.

	Top layer		Layer 2		Layer 3		Layer 4	
	Austenite	Ferrite	Austenite	Ferrite	Austenite	Ferrite	Austenite	Ferrite
Mean von Mises stress (MPa)	694	761	784	846	709	793	694	749
Mean equivalent plastic strain	0.089	0.050	0.079	0.048	0.083	0.043	0.077	0.056
$\sigma_\gamma/\sigma_\alpha$	0.91		0.93		0.89		0.93	
$\varepsilon_\gamma/\varepsilon_\alpha$	1.76		1.66		1.95		1.39	

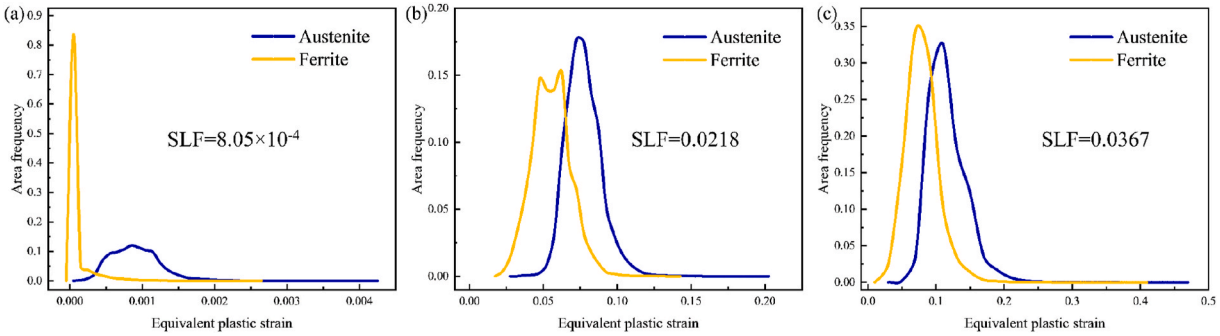

Fig. 9. The curves of PDF of equivalent plastic strain in Layer 4 and the corresponding SLF under three applied strain levels of (a) 0.38%, (b) 7.68%, (c) 11.43%.

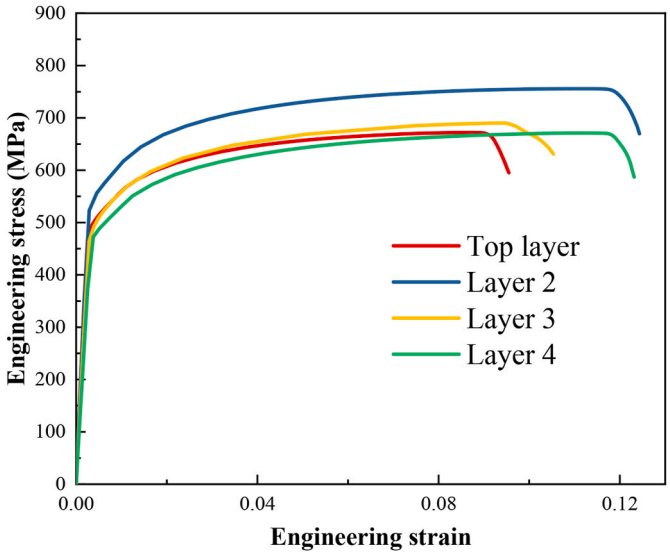

Fig. 10. Engineering strain-stress curves of the four layers obtained by the FEM model.

Table 5
Overall mechanical properties of each layer are exacted by the tensile tests in the FEM model.

	Top layer	Layer 2	Layer 3	Layer 4
E (GPa)	201	194	162	148
σ_y (MPa)	487	535	498	478
Failure strain	0.087	0.111	0.095	0.113
SLF at failure point	0.0465	0.0525	0.0531	0.0367

different in the four layers. The austenite volume fraction in Top layer is the lowest since there is austenite growth in the reheated layers. The complex thermal cycles and cooling rate during the AM process lead to the evolution of the austenite volume fraction.

(2) The results of nanohardness and elastic modulus of the two constituent phases in the four layers show that the values of the hardness and elastic modulus vary significantly from layer to layer, Layer 2 has the highest nanohardness and Top layer has the largest value of elastic modulus. Indentation size effect (ISE) is investigated in the four layers, the obtained value of H_0 in Layer 2 is the largest. The yield strength and strain-hardening exponent are also estimated by the reverse analysis method to obtain the stress-strain behavior of the individual constituent phase.

(3) Then the actual microstructure-based FEM is performed to predict the overall stress and strain behavior of each layer, the distributions of the stress and strain and evolution during the deformation process were examined. All of the simulated overall values of elastic moduli and yield strength show that the trends are in good agreement with the results of nanoindentation tests for individual phases. The trend of failure follows the opposite trend of yield strength except Layer 4 owing to its lower strain localization factor.

Although the studying material and the corresponding FEM models in the current work consist of only two phases, this framework can be utilized in more complex multiphase materials. The current work can be regarded as the pilot for further work on AM-ed multiphase materials. The results of this work provide a great potential application for characterizing the non-uniform materials and small components that do not allow the use of the conventional tensile tests, which is beneficial to improve the structure and mechanical design in the AM industry. Furthermore, this method can not only obtain the overall stress-strain behavior of the specific positions, but also illustrate the distributions of the stress and strain during the deformation process, which demonstrate the effects of the constituent phases in multiphase materials on the resulting mechanical behaviors. The obtained results can be easily used to optimize the AM process and prepare the AM-ed multiphase materials with target mechanical properties. This work focuses on only four layers in the deposition wall, but future studies on other representative locations of the deposition wall will proceed to clarify the specific effects of the thermal cycles in AM process.

CRediT authorship contribution statement

Siqi Liu: Conceptualization, Methodology, Investigation, Writing – original draft, Writing – review & editing, Formal analysis, Visualization, Validation. **Meichao Lin:** Methodology, Formal analysis, Investigation, Writing – review & editing. **Xu Wang:** Investigation. **Yuequn Fu:** Writing – review & editing, Formal analysis. **Xiaobo Ren:** Resources, Writing – review & editing. **Zhiliang Zhang:** Writing – review & editing, Supervision. **Jianying He:** Validation, Writing – review & editing, Supervision, Funding acquisition.

Declaration of competing interest

The authors declare that they have no known competing financial interests or personal relationships that could have appeared to influence the work reported in this paper.

Acknowledgments

The Research Council of Norway (Grant No. 251068) and the Chinese Scholarship Council are acknowledged for the support of this work.

Appendix A. Supplementary data

Supplementary data to this article can be found online at https://doi.

org/10.1016/j.msea.2021.142367.

References

[1] T. DebRoy, H.L. Wei, J.S. Zuback, T. Mukherjee, J.W. Elmer, J.O. Milewski, A. M. Beese, A. Wilson-Heid, A. De, W. Zhang, Additive manufacturing of metallic components – process, structure and properties, Prog. Mater. Sci. 92 (2018) 112–224, https://doi.org/10.1016/j.pmatsci.2017.10.001.

[2] D. Herzog, V. Seyda, E. Wycisk, C. Emmelmann, Additive manufacturing of metals, Acta Mater. 117 (2016) 371–392, https://doi.org/10.1016/j.actamat.2016.07.019.

[3] S. Liu, D. Wan, S. Guan, Y. Fu, X. Ren, Z. Zhang, J. He, Microstructure and nanomechanical behavior of an additively manufactured (CrCoNiFe)94Ti2Al4 high-entropy alloy, Mater. Sci. Eng. 823 (2021) 141737, https://doi.org/10.1016/J.MSEA.2021.141737.

[4] T.D. Ngo, A. Kashani, G. Imbalzano, K.T.Q. Nguyen, D. Hui, Additive manufacturing (3D printing): a review of materials, methods, applications and challenges, Compos. B Eng. 143 (2018) 172–196, https://doi.org/10.1016/j.compositesb.2018.02.012.

[5] W.E. Frazier, Metal additive manufacturing: a review, J. Mater. Eng. Perform. 23 (2014) 1917–1928, https://doi.org/10.1007/s11665-014-0958-z.

[6] L. Sun, X. Ren, J. He, J.S. Olsen, S. Pallaspuro, Z. Zhang, A new method to estimate the residual stresses in additive manufacturing characterized by point heat source, Int. J. Adv. Manuf. Technol. 105 (2019) 2415–2429, https://doi.org/10.1007/S00170-019-04443-1, 2019 1055.

[7] M. Lervåg, C. Sørensen, A. Robertstad, B.M. Brønstad, B. Nyhus, M. Eriksson, R. Aune, X. Ren, O.M. Akselsen, I. Bunaziv, Additive manufacturing with superduplex stainless steel wire by cmt process, Metals 10 (2020) 5–12, https://doi.org/10.3390/met10020272.

[8] B. Wu, Z. Pan, D. Ding, D. Cuiuri, H. Li, J. Xu, J. Norrish, A review of the wire arc additive manufacturing of metals: properties, defects and quality improvement, J. Manuf. Process. 35 (2018) 127–139, https://doi.org/10.1016/j.jmapro.2018.08.001.

[9] K.S. Derekar, A review of wire arc additive manufacturing and advances in wire arc additive manufacturing of aluminium, Mater. Sci. Technol. 34 (2018) 895–916, https://doi.org/10.1080/02670836.2018.1455012.

[10] T.A. Rodrigues, V. Duarte, J.A. Avila, T.G. Santos, R.M. Miranda, J.P. Oliveira, Wire and arc additive manufacturing of HSLA steel: effect of thermal cycles on microstructure and mechanical properties, Addit, Manuf 27 (2019) 440–450, https://doi.org/10.1016/j.addma.2019.03.029.

[11] G. Posch, K. Chladil, H. Chladil, Material properties of CMT—metal additive manufactured duplex stainless steel blade-like geometries, Weld. World 61 (2017) 873–882, https://doi.org/10.1007/s40194-017-0474-5.

[12] Z. Wang, T.A. Palmer, A.M. Beese, Effect of processing parameters on microstructure and tensile properties of austenitic stainless steel 304L made by directed energy deposition additive manufacturing, Acta Mater. 110 (2016) 226–235, https://doi.org/10.1016/j.actamat.2016.03.019.

[13] H. Attar, M.J. Bermingham, S. Ehtemam-Haghighi, A. Dehghan-Manshadi, D. Kent, M.S. Dargusch, Evaluation of the mechanical and wear properties of titanium produced by three different additive manufacturing methods for biomedical application, Mater. Sci. Eng. 760 (2019) 339–345, https://doi.org/10.1016/j.msea.2019.06.024.

[14] J.J. Lewandowski, M. Seifi, Metal additive manufacturing: a review of mechanical properties, Annu. Rev. Mater. Res. 46 (2016) 151–186, https://doi.org/10.1146/annurev-matsci-070115-032024.

[15] C.V. Haden, G. Zeng, F.M. Carter, C. Ruhl, B.A. Krick, D.G. Harlow, Wire and arc additive manufactured steel: tensile and wear properties, Addit. Manuf. 16 (2017) 115–123, https://doi.org/10.1016/j.addma.2017.05.010.

[16] Z. Li, T. Voisin, J.T. McKeown, J. Ye, T. Braun, C. Kamath, W.E. King, Y.M. Wang, Tensile properties, strain rate sensitivity, and activation volume of additively manufactured 316L stainless steels, Int. J. Plast. 120 (2019) 395–410, https://doi.org/10.1016/j.ijplas.2019.05.009.

[17] S. Pathak, S.R. Kalidindi, Spherical nanoindentation stress-strain curves, Mater. Sci. Eng. R Rep. 91 (2015) 1–36, https://doi.org/10.1016/j.mser.2015.02.001.

[18] B. Xu, X. Chen, Determining engineering stress-strain curve directly from the load-depth curve of spherical indentation test, J. Mater. Res. 25 (2010) 2297–2307, https://doi.org/10.1557/jmr.2010.0310.

[19] M.Y. Seok, Y.J. Kim, I.C. Choi, Y. Zhao, J. Il Jang, Predicting flow curves of two-phase steels from spherical nanoindentation data of constituent phases: Isostrain method vs. non-isostrain method, Int. J. Plast. 59 (2014) 108–118, https://doi.org/10.1016/j.ijplas.2014.03.013.

[20] M. Zhao, N. Ogasawara, N. Chiba, X. Chen, A new approach to measure the elastic-plastic properties of bulk materials using spherical indentation, Acta Mater. 54 (2006) 23–32, https://doi.org/10.1016/j.actamat.2005.08.020.

[21] J.L. Bucaille, S. Stauss, E. Felder, J. Michler, Determination of plastic properties of metals by instrumented indentation using different sharp indenters, Acta Mater. 51 (2003) 1663–1678, https://doi.org/10.1016/S1359-6454(02)00568-2.

[22] L. Wang, M. Ganor, S.I. Rokhlin, Inverse scaling functions in nanoindentation with sharp indenters: determination of material properties, J. Mater. Res. 20 (2005) 987–1001, https://doi.org/10.1557/JMR.2005.0124.

[23] M. Dao, N. Chollacoop, K.J. Van Vliet, T.A. Venkatesh, S. Suresh, Computational modeling of the forward and reverse problems in instrumented sharp indentation, Acta Mater. 49 (2001) 3899–3918, https://doi.org/10.1016/S1359-6454(01)00295-6.

[24] X. Long, Q.P. Jia, Z. Li, S.X. Wen, Reverse analysis of constitutive properties of sintered silver particles from nanoindentations, Int. J. Solid Struct. 191–192 (2020) 351–362, https://doi.org/10.1016/j.ijsolstr.2020.01.014.

[25] M.D. Taylor, K.S. Choi, X. Sun, D.K. Matlock, C.E. Packard, L. Xu, F. Barlat, Correlations between nanoindentation hardness and macroscopic mechanical properties in DP980 steels, Mater. Sci. Eng. 597 (2014) 431–439, https://doi.org/10.1016/j.msea.2013.12.084.

[26] G. Cheng, F. Zhang, A. Ruimi, D.P. Field, X. Sun, Quantifying the effects of tempering on individual phase properties of DP980 steel with nanoindentation, Mater. Sci. Eng. 667 (2016) 240–249, https://doi.org/10.1016/j.msea.2016.05.011.

[27] Y. Mazaheri, A. Kermanpur, A. Najafizadeh, Nanoindentation study of ferrite-martensite dual phase steels developed by a new thermomechanical processing, Mater. Sci. Eng. 639 (2015) 8–14, https://doi.org/10.1016/j.msea.2015.04.098.

[28] H. Ghassemi-Armaki, R. Maaß, S.P. Bhat, S. Sriram, J.R. Greer, K.S. Kumar, Deformation response of ferrite and martensite in a dual-phase steel, Acta Mater. 62 (2014) 197–211, https://doi.org/10.1016/j.actamat.2013.10.001.

[29] S.C. Schwarm, R.P. Kolli, E. Aydogan, S. Mburu, S. Ankem, Characterization of phase properties and deformation in ferritic-austenitic duplex stainless steels by nanoindentation and finite element method, Mater. Sci. Eng. 680 (2017) 359–367, https://doi.org/10.1016/j.msea.2016.10.116.

[30] X. Zhang, K. Wang, Q. Zhou, J. Ding, S. Ganguly, M. Grasso, D. Yang, X. Xu, P. Dirisu, S.W. Williams, Microstructure and mechanical properties of TOP-TIG-wire and arc additive manufactured super duplex stainless steel (ER2594), Mater. Sci. Eng. 762 (2019) 138097, https://doi.org/10.1016/J.MSEA.2019.138097.

[31] J. Stützer, T. Totzauer, B. Wittig, M. Zinke, S. Jüttner, GMAW cold wire technology for adjusting the ferrite–austenite ratio of wire and arc additive manufactured duplex stainless steel components, Metals 9 (2019) 564, https://doi.org/10.3390/met9050564.

[32] F. Hejripour, F. Binesh, M. Hebel, D.K. Aidun, Thermal modeling and characterization of wire arc additive manufactured duplex stainless steel, J. Mater. Process. Technol. 272 (2019) 58–71, https://doi.org/10.1016/j.jmatprotec.2019.05.003.

[33] S. Uusikallio, A. Kisko, T.T. Nyo, D.A. Porter, J. Kömi, M. Jaskari, Sample preparation challenges with highly metastable ferritic-austenitic stainless steels, Prakt. Metallogr. Metallogr. 56 (2019) 373–392, https://doi.org/10.3139/147.110580.

[34] A. Laukkanen, S. Uusikallio, M. Lindroos, T. Andersson, J. Kömi, D. Porter, Micromechanics driven design of ferritic–austenitic duplex stainless steel microstructures for improved cleavage fracture toughness, Eng. Fract. Mech. 253 (2021) 107878, https://doi.org/10.1016/j.engfracmech.2021.107878.

[35] K. Holmberg, A. Laukkanen, A. Ghabchi, M. Rombouts, E. Turunen, R. Waudby, T. Suhonen, K. Valtonen, E. Sarlin, Computational modelling based wear resistance analysis of thick composite coatings, Tribol. Int. 72 (2014) 13–30, https://doi.org/10.1016/J.TRIBOINT.2013.12.001.

[36] L.Q. Guo, M.C. Lin, L.J. Qiao, A.A. Volinsky, Ferrite and austenite phase identification in duplex stainless steel using SPM techniques, Appl. Surf. Sci. 287 (2013) 499–501, https://doi.org/10.1016/j.apsusc.2013.09.041.

[37] M.C. Lin, G. Wang, L.Q. Guo, L.J. Qiao, A.A. Volinsky, Electro-mechanical coupling of semiconductor film grown on stainless steel by oxidation, Appl. Phys. Lett. 103 (2013) 143118, https://doi.org/10.1063/1.4824072.

[38] X. Zhang, K. Wang, Q. Zhou, J. Ding, S. Ganguly, M. Grasso, D. Yang, X. Xu, P. Dirisu, S.W. Williams, Microstructure and mechanical properties of TOP-TIG-wire and arc additive manufactured super duplex stainless steel (ER2594), Mater. Sci. Eng. 762 (2019), https://doi.org/10.1016/j.msea.2019.138097.

[39] W.C. Oliver, G.M. Pharr, An improved technique for determining hardness and elastic modulus using load and displacement sensing indentation experiments, J. Mater. Res. 7 (1992) 1564–1583, https://doi.org/10.1557/jmr.1992.1564.

[40] W.C. Oliver, G.M. Pharr, Measurement of hardness and elastic modulus by instrumented indentation: advances in understanding and refinements to methodology, J. Mater. Res. 19 (2004) 3–20, https://doi.org/10.1557/jmr.2004.19.1.3.

[41] K.R. Gadelrab, G. Li, M. Chiesa, T. Souier, Local characterization of austenite and ferrite phases in duplex stainless steel using MFM and nanoindentation, J. Mater. Res. 27 (2012) 1573–1579, https://doi.org/10.1557/jmr.2012.99.

[42] C.H. Hsueh, M.J. Liao, S.H. Wang, Y.T. Tsai, J.R. Yang, R. Wu, W.S. Lee, Size effect and strain induced double twin by nanoindentation in DSS weld metal of vibration-assisted GTAW, Mater. Chem. Phys. 219 (2018) 40–50, https://doi.org/10.1016/j.matchemphys.2018.07.055.

[43] F. Khodabakhshi, M.H. Farshidianfar, A.P. Gerlich, M. Nosko, V. Trembošová, A. Khajepour, Microstructure, strain-rate sensitivity, work hardening, and fracture behavior of laser additive manufactured austenitic and martensitic stainless steel structures, Mater. Sci. Eng. 756 (2019) 545–561, https://doi.org/10.1016/j.msea.2019.04.065.

[44] W.D. Nix, H. Gao, Indentation size effects in crystalline materials: a law for strain gradient plasticity, J. Mech. Phys. Solid. 46 (1998) 411–425, https://doi.org/10.1016/S0022-5096(97)00086-0.

[45] G.M. Pharr, E.G. Herbert, Y. Gao, The indentation size effect: a critical examination of experimental observations and mechanistic interpretations, Annu. Rev. Mater. Res. 40 (2010) 271–292, https://doi.org/10.1146/annurev-matsci-070909-104456.

[46] C. Yan, R. Wang, Y. Wang, X. Wang, Z. Lin, G. Bai, Y. Zhang, Size effects in indentation measurements of Zr-1Nb-0.05Cu alloy, Mater. Sci. Eng. 628 (2015) 50–55, https://doi.org/10.1016/j.msea.2015.01.024.

[47] P. Tao, J. ming Gong, Y. fei Wang, Y. Jiang, Y. Li, W. wei Cen, Characterization on stress-strain behavior of ferrite and austenite in a 2205 duplex stainless steel based

on nanoindentation and finite element method, Results Phys 11 (2018) 377–384, https://doi.org/10.1016/j.rinp.2018.06.023.
[48] Z. Hu, K. Lynne, F. Delfanian, Characterization of materials' elasticity and yield strength through micro-/nano-indentation testing with a cylindrical flat-tip indenter, J. Mater. Res. 30 (2015) 578–591, https://doi.org/10.1557/jmr.2015.4.
[49] D. Tabor, The hardness of metals, Oxford Univ. Press, 2000. https://global.oup.com/academic/product/the-hardness-of-metals-9780198507765?cc=no&lang=en&. (Accessed 2 January 2021).
[50] R. Rodríguez, I. Gutierrez, Correlation between nanoindentation and tensile properties influence of the indentation size effect, Mater. Sci. Eng. 361 (2003) 377–384, https://doi.org/10.1016/S0921-5093(03)00563-X.
[51] Z.S. Ma, Y.C. Zhou, S.G. Long, C.S. Lu, An inverse approach for extracting elastic-plastic properties of thin films from small scale sharp indentation, J. Mater. Sci. Technol. 28 (2012) 626–635, https://doi.org/10.1016/S1005-0302(12)60108-X.
[52] M. Dao, N. Chollacoop, K.J. Van Vliet, T.A. Venkatesh, S. Suresh, Computational modeling of the forward and reverse problems in instrumented sharp indentation, Acta Mater. 49 (2001) 3899–3918, https://doi.org/10.1016/S1359-6454(01)00295-6.
[53] R. Shi, Z. Nie, Q. Fan, G. Li, Elastic plastic deformation of TC6 titanium alloy analyzed by in-situ synchrotron based X-ray diffraction and microstructure based finite element modeling, J. Alloys Compd. 688 (2016) 787–795, https://doi.org/10.1016/j.jallcom.2016.07.105.
[54] Z. tao Zhao, X. song Wang, G. ying Qiao, S. yu Zhang, B. Liao, F. ren Xiao, Effect of bainite morphology on deformation compatibility of mesostructure in ferrite/bainite dual-phase steel: mesostructure-based finite element analysis, Mater. Des. 180 (2019) 107870, https://doi.org/10.1016/j.matdes.2019.107870.
[55] H. Hosseini-Toudeshky, B. Anbarlooie, J. Kadkhodapour, Micromechanics stress-strain behavior prediction of dual phase steel considering plasticity and grain boundaries debonding, Mater. Des. 68 (2015) 167–176, https://doi.org/10.1016/j.matdes.2014.12.013.